Multi-kHz temperature imaging in turbulent non-premixed flames using planar Rayleigh scattering

R.A. Patton · K.N. Gabet · N. Jiang · W.R. Lempert · J.A. Sutton

Abstract In this manuscript, we describe the development of two-dimensional, high-repetition-rate (10-kHz) Rayleigh scattering imaging as applied to turbulent combustion environments. In particular, we report what we believe to be the first sets of high-speed planar Rayleigh scattering images in turbulent non-premixed flames, yielding temporally correlated image sequences of the instantaneous temperature field. Sample results are presented for the well-characterized DLR flames A and B ($CH_4/H_2/N_2$) at Reynolds numbers of 15,200 and 22,800 at various axial positions downstream of the jet exit. The measurements are facilitated by the use of a user-calibrated, intensified, high-resolution CMOS camera in conjunction with a unique high-energy, high-repetition-rate pulse-burst laser system (PBLS) at Ohio State University, which yields output energies up to 200 mJ/pulse at 532 nm with 100-μs laser pulse spacing. The spatial and temporal resolution of the imaging system and acquired images are compared to the finest spatial and temporal scales expected within the turbulent flames. One of the most important features of the PBLS is the ability to readily change the pulse-to-pulse spacing as the required temporal resolution necessitates it. The quality and accuracy of the high-speed temperature imaging results are assessed by comparing derived statistics (mean and standard deviation) to that of previously reported point-based reference data acquired at Sandia National Laboratories and available within the TNF workshop. Good agreement between the two data sets is obtained providing an initial indication of quantitative nature of the planar, kHz-rate temperature imaging results.

1 Introduction

Turbulent combustion processes account for more than 85% of the world's energy usage with applications ranging from power generation to aviation propulsion. It is expected that the requirements for the next generation of energy-conversion systems will include significant improvements in overall efficiency both in terms of performance and decreased emission output. In order to satisfy both of these stringent demands, new and improved understanding of fundamental combustion chamber processes including fluid mechanics, reactant mixing, ignition, turbulence-chemistry interactions, and the subsequent finite-rate chemical processes such as pollutant formation will be required through advanced experimentation. The use of laser diagnostics already have played a primary role in elucidating some of the pertinent physical and chemical processes occurring within highly turbulent reacting environments, including the investigation of flame structure, species concentration distributions, temperature, and turbulence characteristics. Such measurement techniques have yielded previously unknown information regarding the interaction between turbulent fluid mechanics and finite-rate combustion chemistry; information that has impacted several specific engineering disciplines including gas turbine and automotive research.

One quantity that is of particular importance for characterizing turbulent combustion environments is the instantaneous, time-varying temperature field. Temperature distributions play a critical role in the governing chemical (i.e., reaction rates) and physical (i.e., heat transfer, gas expansion) processes that occur in combustion environments. For

R.A. Patton · K.N. Gabet · N. Jiang · W.R. Lempert ·
J.A. Sutton (✉)
Department of Mechanical and Aerospace Engineering, The Ohio State University, E447 Scott Laboratory, 201 West 19th Avenue, Columbus, OH 43210, USA
e-mail: sutton.235@osu.edu
Fax: +1-614-2923163

example, the local flame temperature is a primary factor in controlling ignition and flame kernel growth, local flame extinction and re-ignition, and soot and NO_x formation. Also, it can be argued that the thermal field is inherently linked and strongly correlated with the turbulent mixing field, at least in flame cases far from extinction. For non-premixed and partially premixed systems, the mixture fraction (ξ) and the scalar dissipation rate [$\chi = 2D(\nabla \xi \cdot \nabla \xi)$] are fundamental quantities that describe the state and rate of molecular mixing within the turbulent flames e.g., [1–3]. The rate of mixing, as determined from χ, governs the rate of chemical reaction in turbulent flames. In operating cases away from extinction, the state relation, $T = T(\xi)$ typically is exhibited, which implies that the rate of thermal mixing is related to and proportional to the scalar dissipation rate e.g., [4, 5]. Thus, measurements of the temperature field (and its derivatives) not only yield information on the thermal mixing, but some information on the underlying structure of the molecular mixing processes as well.

Over the last three decades, numerous approaches to laser-based thermometry have been developed and applied in high-temperature, reacting flows including Rayleigh scattering, spontaneous Raman scattering, laser-induced fluorescence, coherent anti-Stokes Raman scattering, thermographic phosphorescence, and absorption-based approaches. The fundamentals, specific details, and examples of each of these approaches can be found in several comprehensive review articles and texts e.g., [6–14]. For highly turbulent systems, planar temperature measurements are highly desired in order to spatially resolve the complex physical structures within the turbulent flames. Of the aforementioned laser-based approaches, planar laser-induced fluorescence (PLIF), based on the simultaneous excitation of two wavelengths (i.e., "two-line thermometry") e.g., [15–18] and planar Rayleigh scattering e.g., [7–9, 19] are the most readily used techniques for multi-dimensional temperature imaging.

The first applications of Rayleigh scattering imaging for thermometry were demonstrated in the late 1970s and early 1980s by Pitz et al. [20], Smith [21] and Dibble and Hollenbach [22], who performed 0D and 1D temperature measurements in turbulent flames, while the first two-dimensional Rayleigh scattering temperature imaging was performed by Long and co-workers in 1985/1986 [23, 24]. In the last 25 years, planar Rayleigh scattering has been widely used for instantaneous two- and three-dimensional measurements of the temperature field in turbulent premixed, partially premixed, and non-premixed flames (see Ref. [8] for many examples within laboratory-scale and practical configurations). While many previous measurements have been performed with very high spatial resolution in multiple dimensions, they have not been performed at acquisition rates high enough to resolve the time-varying nature of the flowfield. Recognizing that turbulence is inherently stochastic,

the flowfield scalars such as temperature should be resolved in both space and time in order to capture the dynamic nature of turbulent flames. This requirement dictates that the data acquisition rate of the scalar fields is much greater than typical time scales of the turbulent processes ($\gg 1$ kHz). Typical signal levels for gas-phase scattering measurements are sufficiently small such that high-power, pulsed laser sources are required. Commercially available high-energy systems including Q-switched solid-state lasers such as Nd:YAG or gas lasers such as excimers are limited to pulse repetition-rates of 10 to 300 Hz. In this manner, previous multi-dimensional temperature measurements using Rayleigh scattering have been limited in temporal resolution, that is, any two consecutive images have been temporally uncorrelated.

In this study, we will describe the use of pulse-burst laser technology e.g., [25–30] to produce a series of high-energy laser pulses that can be used for high-speed (>10-kHz) planar Rayleigh scattering imaging. Specifically, this work will focus on using Rayleigh scattering as an approach to measuring temporally correlated 2D image sequences of the temperature field in turbulent non-premixed jet flames. The combination of high pulse energies and a user-calibrated, intensified, high-speed CMOS camera results in high-quality, quantitative image sequences of the two-dimensional temperature field. To the authors' knowledge, these are the first sets of high-speed 2D Rayleigh scattering images in turbulent flames, which resolve the temporally fluctuating nature of the temperature field and thermal mixing.

2 Previous high-speed imaging and kHz-rate temperature measurements

The recent advances in solid-state diode-pumped lasers and CMOS sensor-based camera technology has permitted some common laser imaging techniques such as particle imaging velocimetry (PIV), planar laser-induced fluorescence (PLIF), and laser-induced incandescence (LII) to be demonstrated effectively at multi-kilohertz acquisition rates e.g., [31–50]. However, these measurement approaches all require low individual pulse energies (<10 mJ), which are conducive to using commercially available high-repetition rate laser systems. While high-speed PIV and OH PLIF imaging are becoming more common, the "real time" measurement of other scalar quantities proves much more difficult due to pulse energy limitations of current commercially available laser technology, which for solid-state lasers is primarily dictated by thermal loading capacity. The low pulse energies available from commercially available systems are not only prohibitive to Raman and Rayleigh scattering diagnostics, but potentially to PLIF imaging of other reactive species that are common at low repetition rates (e.g., CH, NO, CH_2O).

As an alternative to a continuous duty cycle, previous authors have demonstrated the ability to generate a limited number of higher-energy pulses at high-repetition rates. Initial work at Lund University consisted of "clustering" conventional Nd:YAG and ICCD camera technology to capture up to eight sequential images of the OH and CH_2O concentration fields via PLIF during transient events such as ignition and local flame extinction e.g., [51–58]. As one example, starting with 270 mJ per pulse at 532 nm, they were able to generate eight pulses at 282 nm for OH PLIF measurements, with pulse energies of 1 mJ and a minimum inter-pulse period of 125 µs, constrained by the high-intensity pumping requirement of the dye laser. Recently, Sjöholm et al. [59] used the same laser system to pump an optical parametric oscillator (OPO) system and frequency-double the output for OH PLIF measurements, thus overcoming the inter-pulse spacing limitation imposed by the use of a dye laser. However, an additional limitation of this "clustered" approach is the number of output pulses available; simply put, increasing the record length of the image sequence requires additional laser sources, which quickly becomes cost prohibitive.

Another well-known approach to making high-speed measurements (over a limited duty cycle) is what has become known as "pulse burst" mode. Wu et al. [60] demonstrated the first generation of this type of pulse-burst laser system by amplifying a low-power continuous wavelength (cw) laser using a conventional flashlamp-pumped amplifier and then forming this one long pulse into a burst of pulses through a Pockels-cell slicer, followed by additional amplifier stages. Subsequently, Lempert et al. [25] and Thurow et al. [61] have developed effective second generation systems, both extending the burst duration and increasing the pulse energies to levels suitable for spectroscopic measurements. As examples of the utility of the PBLS for reacting flow measurements, Miller et al. [26] acquired 20 temporally correlated OH PLIF images at a 50 kHz acquisition rate in a turbulent hydrogen-air diffusion flame and Jiang et al. [29] acquired ten temporally correlated CH PLIF images at 10 kHz in a turbulent $CH_4/H_2/N_2$ flame. The pulse-burst laser system (PBLS) at Ohio State is used in the present study for high-repetition-rate temperature imaging as further described below.

To date, there are only a few reported studies of multi-kilohertz, laser-based temperature measurements in flames. Wang et al. [62–64] reported single- and two-point temperature measurements using Rayleigh scattering at 10-kHz acquisition rates with a 71-W ($\sim$7 mJ/pulse) diode-pumped Nd:YAG laser at 532 nm. These measurements were used to study temperature fluctuations, power spectra, time scales, thermal gradients, and thermal dissipation rate characteristics in a turbulent non-premixed jet-flame (DLR Flame

A [65]). Subsequently, Meyer et al. [66] demonstrated simultaneous single-point OH LIF and temperature measurements using Rayleigh scattering at 100 kHz using a 80-MHz mode-locked Ti:sapphire laser with ultra-short 2 ps pulses with $\sim$1 µJ of pulse energy at 460 nm. These measurements were demonstrated within an unsteady Rolon vortex/flame burner with a reported uncertainty of ±25%. Most recently, Bork et al. [67] successfully demonstrated high-repetition rate 1D Rayleigh scattering thermometry in the DLR Flame A using a commercial, 80-W, diode-pumped Nd:YAG laser operating at 10-kHz in conjunction with an un-intensified CMOS camera and low-f-number optical collection system. While the long record lengths (afforded by the commercial laser systems) presented in the previous work offer some significant advantages, the lower pulse energies (<10 mJ/pulse) are not likely to facilitate the extension of the 0D and 1D measurements to 2D imaging with sufficient signal-to-noise ratios.

3 Experimental methods

3.1 Rayleigh scattering

For low-repetition rate studies, planar Rayleigh scattering has been used extensively for imaging the instantaneous temperature field in turbulent premixed, partially premixed, and non-premixed flames. Laser Rayleigh scattering is a non-intrusive diagnostic technique that describes the scattering from molecules whose effective diameter is much less than the wavelength of the incident laser light, where the Rayleigh scattering intensity can be written as

$$I_{RAY} = A I_o n \sigma_{mix}. \tag{1}$$

In (1), A is a constant describing collection volume and efficiency of the optical setup, I_o is the incident laser intensity, n is the number density, and σ_{mix} is the mixture-averaged differential cross-section defined as $\sigma_{mix} = \sum_{i=1}^{N} X_i \sigma_i$. X_i and σ_i are the mole fraction and differential cross-section of species i, respectively. For low Mach number flows, the ideal gas law, $p = nkT$, where p is the pressure, k is the Boltzmann constant, and T is the temperature can be substituted into (1) yielding

$$I_{RAY} = A I_o \frac{P}{kT} \sigma_{mix}. \tag{2}$$

For flame temperature measurements, the constant A is typically accounted for by normalizing the measured Rayleigh signal to a Rayleigh signal of known temperature and species concentration such as that from air at room temperature. The turbulent non-premixed flames considered in this study are the well-characterized DLR-A and DLR-B flames [65, 68] which are comprised of a fuel mixture of 22.1%

Fig. 1 (**a**) Schematic diagram and optical layout of pulse-burst laser system (PBLS) at OSU. (**b**) A typical ten-pulse laser burst trace at 532 nm with 100 μs inter-pulse spacing (10 kHz acquisition rate). Pulse-to-pulse intensity variations are less than 8%
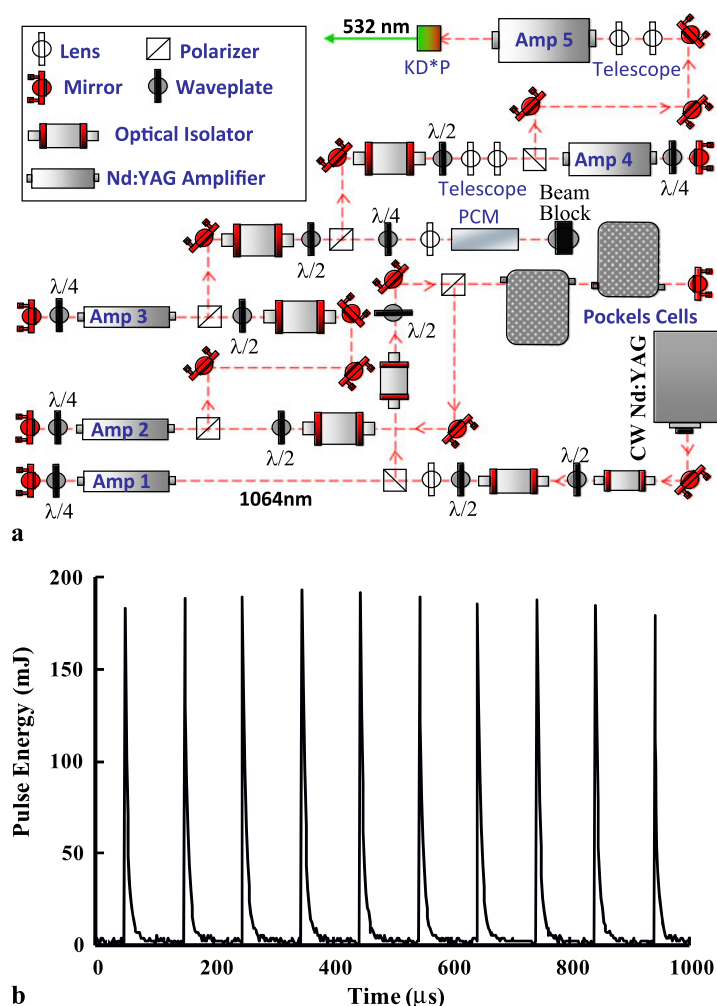
CH$_4$, 33.2% H$_2$, and 44.7% N$_2$. For this fuel combination, the mixture-averaged differential cross-section varies by less than 3% throughout the flame, thus enabling a calculation of the local gas temperature without a need for measuring the local species concentrations. In this manner, the temperature is derived from

$$T = T_{ref} \frac{I_{ref}}{I_{RAY}}, \qquad (3)$$

where I_{ref} is the reference Rayleigh scattering signal from air at room temperature (T_{ref}).

Although frequently utilized at low repetition rates, planar Rayleigh scattering requires high pulse energies (especially for reacting flows with low number densities); pulse energies that currently are not available from commercial high-repetition-rate laser systems. In the next section, we describe a custom pulse-burst laser system at Ohio State that produces a series of high-energy laser pulses with micro-second level temporal spacing, allowing high-speed (multi-kilohertz) planar Rayleigh scattering measurements for quantitative temperature imaging in turbulent non-premixed flames.

3.2 Pulse-burst laser system at OSU

The pulse-burst laser system (PBLS) at Ohio University, shown schematically in Fig. 1(a), has been described in detail previously [25, 27] and thus will only be described briefly here. The laser system is a master oscillator, power amplifier (MOPA) design, which consists of a single-frequency ($<10^{-3}$ cm^{-1}) cw diode-pumped ring laser operating at 1064 nm serving as the primary oscillator, an electro-optic dual Pockels-cell pulse slicer, and a series of flashlamp-pumped Nd:YAG amplifiers. The cw laser is initially pre-amplified in a double-pass variable pulse width ($\sim$1.5 ms in this study) flashlamp-pumped amplifier and then formed into a "burst" of laser pulses by rapidly rotating the polarization of the pre-amplified pulse by one of two Pockels cells as described by Wu et al. [60]. In the present experiment, the slicing process creates a train of 10-ns wide pulses, which are separated by 100 μs, corresponding to a repetition rate of 10 kHz. We note, however, that this system has been used previously at repetition rates up to 1 MHz (pulse separations equal to 1 μs) e.g., [69]. The

pulse train is then further amplified by a series of four additional flashlamp-pumped Nd:YAG amplifiers, resulting in a system gain of $>10^8$. The pulse trains are limited in the present study to 1 ms, which corresponds to ten temporally sequential laser pulses and images.

It is noted that amplifier stages cannot be added to the system arbitrarily as system performance is limited by the onset and growth of Amplified Spontaneous Emission (ASE) in the forward direction. ASE competes with and ultimately limits the achievable laser gain within any high-power laser system. To reduce amplified spontaneous emission (ASE) buildup in the system, a phase conjugate mirror (PCM) is placed between amplification stages 3 and 4 [25]. The PCM is an optical cell filled with a high index-of-refraction liquid (FC-75) that uses the principle of stimulated Brillouin scattering (SBS) to act as an intensity filter and break the unwanted ASE growth. In addition, the SBS PCM eliminates the low-intensity pedestal which is superimposed on the desired pulse-burst sequence because of the finite on/off contrast ratio of the Pockels-cell pulse slicer. When the pump beam intensity is above a minimum threshold, a coherent beam is retro-reflected (with a ∼1 GHz frequency shift) and the desired high-intensity laser burst is backscattered toward the final amplifier stages, while the sources of low-intensity background (e.g., ASE) do not exceed minimum threshold and pass through the PCM cell to a beam dump. Finally, the series of 1064-nm laser pulses are frequency-doubled to 532 nm with a KD*P crystal, which is convectively cooled. In the current work, the individual energies of the 532-nm pulses are approximately 200 mJ. An example series of 532-nm pulses are shown in Fig. 1(b), where the intensity difference between the pulses is less than 8%. Previously, this system has been used to perform high-repetition-rate (10 to 50 kHz) OH and CH PLIF imaging in turbulent flames e.g., [26, 29], NO PLIF imaging in hypersonic flows [27, 69], Raman scattering measurements in isothermal turbulent jets [28], and most recently mixture fraction imaging in turbulent non-reacting jets using planar Rayleigh scattering [30].

3.3 Optical arrangement

A schematic of the optical arrangement used for these experiments is given in Fig. 2. The 532-nm output of the pulse-burst laser system (PBLS) is initially passed through a thin film polarizer (TFP) to ensure that only vertically polarized laser light transmits to the test-section because of the polarization-dependence of Rayleigh scattering. The vertically polarized light (approximately 95% of the initial pulse energy) is formed into a 40×0.16 mm^2 laser sheet via a combination of a single plano-concave cylindrical lens ($f = -100$ mm) and a plano-concave spherical lens ($f = 750$ mm). The laser-sheet thickness (reported as
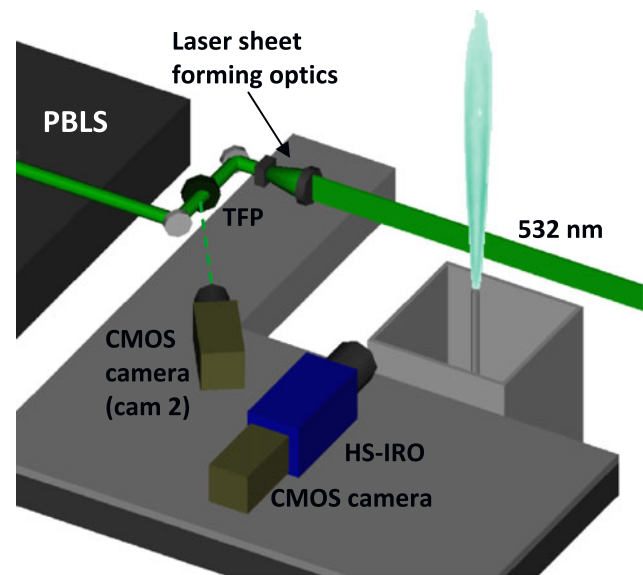

Fig. 2 Overview of the experimental setup for high-speed 2D Rayleigh scattering temperature imaging. The second CMOS camera (cam2) is used for pulse-to-pulse laser energy and intensity distribution corrections. TFP—thin film polarizer

the $1/e^2$ value) was determined by first removing the cylindrical lens and measuring the beam diameter at the focal point of the probe volume using Rayleigh scattering imaging from ambient air. The horizontally polarized component of the laser, which is reflected off of the TFP, is collected by a high-speed CMOS camera outfitted with a 50 mm $f/1.2$ Nikon camera lens to act as a secondary energy monitor for each individual laser pulse.

The high-speed Rayleigh scattering images are collected with a single high-speed CMOS camera (Vision Research, Phantom v710) coupled to a high-speed image intensifier (LaVision Inc., HS-IRO) and outfitted with an 85 mm $f/1.4$ Nikon camera lens operating at 10,000 frames per second with an effective resolution of 1024×664 pixels. The resulting magnification is approximately 1:2.8 with no barrel distortion or spherical aberration and only small levels of vignetting apparent. The total vignetting of an intensified camera originates from the vignetting of the front-end objective, the coupling lenses, and predominately the mechanical vignetting due to a mismatch between intensifier and the camera sensor. In our previous work using only the CMOS camera, no vignetting was apparent [30]. The primary mode of mitigating the total vignetting was to remove the border pixels of the original image before further data processing. As described in Sect. 3.5, a flatfield correction is applied which compensates for the remaining vignetting effects as well as other sources of image non-uniformities. This experimental configuration yields an imaged field-of-view of approximately 57×37 mm^2 (before cropping) with an in-plane spatial resolution of 56 μm (before binning). Thus, the

out-of-plane spatial resolution, as determined by the laser-sheet thickness, determines the limiting spatial resolution of the measurements. The synchronization of the camera acquisition to the PBLS output is controlled using a commercially available high-speed camera controller (HSC, LaVision, Inc.).

3.4 Turbulent non-premixed flame conditions

The turbulent non-premixed flames considered in this study are simple jet-flames issuing into a low-speed co-flow of air ($\sim$0.3 m/s) that serve as benchmark flames in the International Workshop for the Computation of Turbulent Non-premixed Flames (TNF Workshop) [70]. The fuel, which consists of 22.1% CH_4/33.2% H_2 /44.7% N_2, issues from a 8-mm-diameter tube at 43.2 m/s for DLR Flame A and 63.2 m/s for DLR Flame B into the 30×30 cm^2 co-flow. These flow conditions correspond to Reynolds numbers of 15200 and 22800, respectively based on nozzle diameter. Flame A displays low levels of local flame extinction, while Flame B is close to blowoff and displays moderate levels of local extinction [65]. The stoichiometric mixture fraction is 0.167 and the differential Rayleigh scattering cross-section is constant throughout the flame to within $\pm$3% [65, 68], facilitating straight-forward temperature measurements using Rayleigh scattering as described in Sect. 3.1. The co-flowing air is supplied by a forced-air blower (rated at 14 m^3/min), which passes through a series of perforated plates (1 mm hole diameter, 45% open area), a HEPA filter, and a 3-mm hexagonal cell-size honeycomb flow straightening section for flow conditioning and particulate removal, resulting in a particle-free, laminar, uniform co-flow. Particulate filtering (e.g., dust) is absolutely essential because laser Mie scattering from particles can completely mask the Rayleigh scattering signal. The co-flow was found to be particle-free for axial positions up to $x/d = 60$; at this point, dust and other particulate enter the flowfield due to entrainment from the surrounding room air.

3.5 Camera system characterization, image processing, and data reduction

For quantitative temperature field measurements, proper reduction of the acquired Rayleigh scattering signal is paramount. In this work, similar systematic reduction procedures are followed as outlined in Ref. [30], with some alternate steps due to the use of a high-speed image intensifier. The reduction process is as follows: (1) subtraction of background signals (e.g., darkfield image and stray light scattering subtraction), (2) linearization of the camera/intensifier combination, (3) correction for sensor non-uniformity, i.e., "flatfield" corrections, (4) correction for image intensifier charge depletion and image bleed (not observed in current

work, but is required under long record length acquisitions and ultra-high framing rates), (5) correction for shot-to-shot energy fluctuations, (6) correction for the non-uniformity of the laser-sheet intensity distributions, and (7) 3×3 pixel binning to increase the signal-to-noise. The 3×3 binning results in an in-plane spatial resolution ($<$170 μm) which is matched to the out-of-plane spatial resolution defined by the laser-sheet thickness.

As described in several recent publications, CMOS-based camera systems have an independent response for each pixel e.g., [71–73], which may induce varying levels of non-linearity and non-uniformity throughout the acquired image. In addition, the use of an image intensifier may act to enhance these non-ideal attributes and introduce new sources of signal ambiguity such as mechanical vignetting (or shadowing) from the mismatch between photocathode and camera sensor sizes, image bleed from successive frames, and non-uniform, intensity-dependent charge depletion that occurs at high framing rates due to the inability of the intensifier to recharge between successive frames [73]. As shown previously e.g., [30, 73], there is a need to carefully calibrate CMOS and intensified-CMOS cameras for quantitative measurements. Similar to our previous work in non-reacting flows using only a CMOS camera [30], we follow the recent suggestions of Weber et al. [73] by performing a pixel-by-pixel correction for the intensified-CMOS response.

As described in Ref. [30], the linearity, non-uniformity, and charge-depletion characteristics of the intensified CMOS camera system was tested using an experimental setup similar to that described by Hain et al. [72]. For these measurements, a calibrated, Ulbricht sphere (LMT Lichtmesstechnik; Berlin, Germany) was used as the illumination source as depicted in Fig. 3(a). This Ulbricht sphere has a diffusing screen radius (r) of 35 mm and provides a well-defined light source with non-uniformities of less than 0.1% over the entire aperture. The incident illuminance E (lux) to the photocathode of the intensifier is calculated as [72]

$$E = \frac{\pi r^2}{r^2 + d^2} L \tag{4}$$

where d is the distance between the intensifier and the Ulbricht sphere as shown in Fig. 3(a) and L is the luminance (candela/m^2) of the Ulbricht sphere (at the diffusing screen). In this manner, the luminance level at the photocathode can be varied by adjusting d, that is, the distance between the image intensifier/CMOS camera system and the Ulbricht sphere. This was accomplished by mounting the intensified-CMOS camera system on a precision optical rail and systematically increasing (or decreasing) d in known increments with an accuracy of 0.5 mm. For these experiments, the intensifier is illuminated directly by the Ulbricht sphere without a camera lens and without any additional ambient light (i.e. a dark room). It should be noted that a constant gain setting (55% of the maximum multi-channel
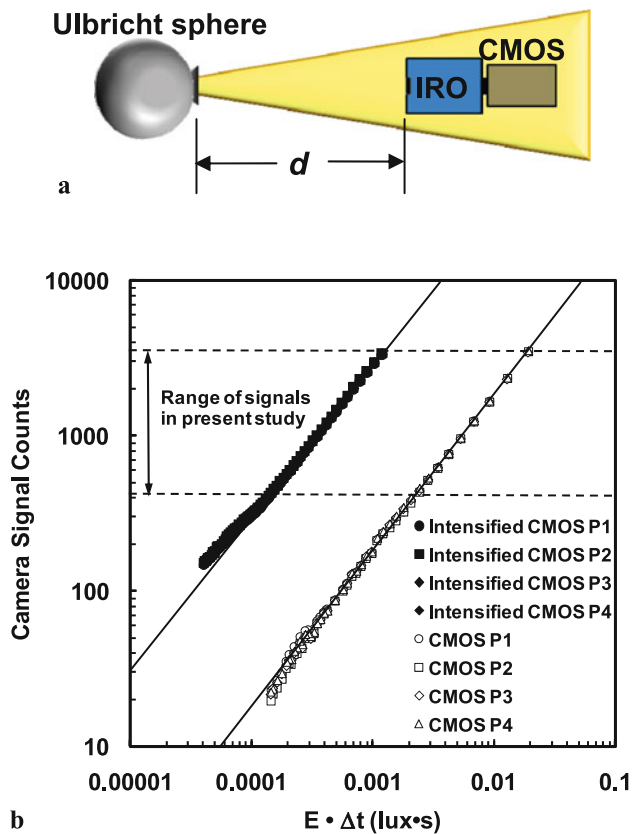
Fig. 3 (**a**) Schematic of the test setup for determining the linearity and uniformity of the high-speed intensified CMOS camera system. (**b**) Linearity results depicting the dependence on the acquired signal (displayed in terms of signal counts) on $E \cdot \Delta t$. The four camera pixels (P1–P4) correspond to image (x, y) coordinates of $(256, 166)$, $(256, 768)$, $(498, 166)$, and $(498, 166)$, respectively. Also shown (for comparison) are the linearity results from the un-intensified CMOS camera from Ref. [30] using the same four pixels

Fig. 4 (**a**) Lineplot at pixel 332 in the vertical direction from a 250-shot average intensified-CMOS camera (*red line*) depicting the degree of image non-uniformity. For comparison, the results from an un-intensified CMOS camera image (*black line*) are shown. (**b**) Probability density function (PDF) of normalized signal levels (S/S_{avg}) for three instantaneous images with varying levels of signal ($S_{avg} = 1000$, 2000, and 3500) showing the degree of sensor (*image*) non-uniformity is independent of incident intensity (and corresponding camera signal)

plate, MCP, voltage) was used for all system characterization, which matched the conditions used for the temperature imaging described below. This gain setting resulted in an overall signal gain (as compared to the camera without an intensifier) of 15. This relatively low gain (compared to typical intensifier operating conditions) allows the camera system to still operate with sufficiently high dynamic range (>100) since it is known that the dynamic range of a camera scales inversely with the camera system gain.

The linearity of the intensified-CMOS camera system used in this work is shown in Fig. 3(b). Each data point represents the average of 250 images (7 µs gate) after subtraction of the average background signal. Results are shown for four separate pixels (specified in the caption), although we note that results for all 1024×664 pixels are used for the image processing. Also shown in Fig. 3(b) are the recent results using only the CMOS camera (no intensifier) for the same pixel locations [30]. The linear range covers more than two orders of magnitude, where only the lower 7% of the camera's signal range departs from the apparent linear
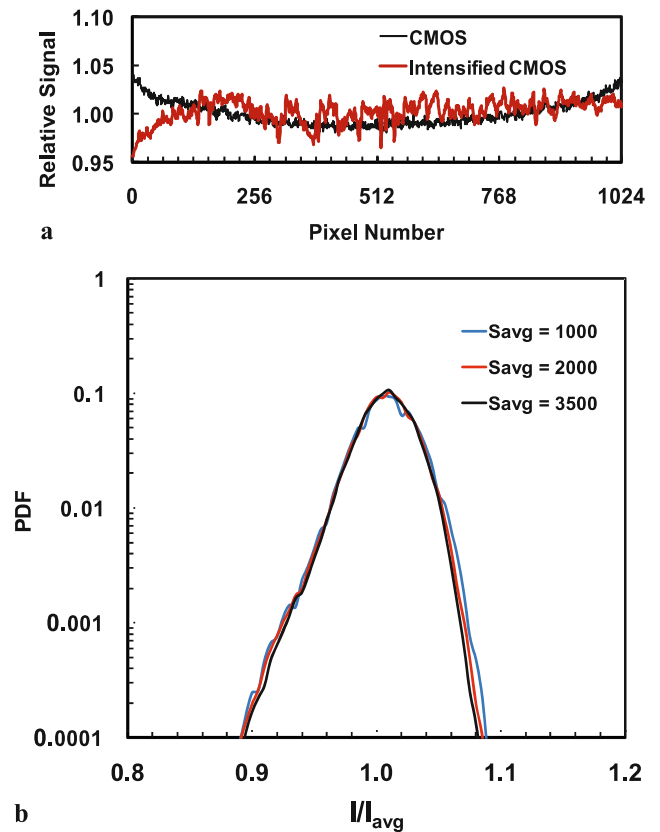
behavior. However, this is not necessarily an indication of non-linear effects. The somewhat abrupt departure from the linear curve occurs at a ($E \cdot \Delta t$) of approximately 10^{-4} lux/s or a detected signal level of ~ 300 counts. At this point, the entire camera and rail system was re-positioned (as opposed to simply translating the camera) in order to realize larger distances (d) between the Ulbricht sphere and intensified camera system. Similar results were noted in Ref. [72] that attributed this change in linearity characteristics to the mean grey value of the intensified camera system increasing over the longer duration needed to re-position the entire system (tens of minutes) versus simple camera translation (tens of seconds). In any regard, these signal levels were not encountered in the temperature imaging results described below and therefore do not affect the linearity correction that is based on the results from ($E \cdot \Delta t$) of 2×10^{-4} to 2×10^{-3} lux/sec (400 to 4000 signal counts).

The same experimental setup and data obtained from using the Ulbricht sphere also are used for corrections for sensor non-uniformity (i.e., the "whitefield" response func-

tion). Figure 4(a) shows a typical intensity profile obtained at a vertical location corresponding to pixel 332 (of 664) from an average of 250 images with incident $E \cdot \Delta t$ of $\sim 1 \times 10^{-3}$ lux/sec (signal level ~ 3000 counts). It is observed that the image is fairly uniform with a $\pm 3\%$ departure from the row-averaged signal level. The most significant levels of non-uniformity occur at the edges of the image, which are due to vignetting effects as previously discussed. However, it is noted that these regions of the images are not used in the final reduced data sets. As expected, the noise level (or fluctuation in image uniformity) is greater when using the intensifier versus the results using the CMOS camera alone.

When using a high-speed image intensifier, it is important to verify that the image corrections obtained at a single (N-image-averaged) signal level are applicable over all possible measured signal levels occurring within instantaneous images, which for CCD (and CMOS sensors alone) is largely the case. Figure 4(b) shows the probability density function (PDF) of acquired signal levels (S) for three instantaneous images, normalized by the average signal level of that particular image (S_{avg}), which were 1000, 2000, and 3500 counts, respectively. Two important features from the PDFs are noted: (1) The degree of departure from the individual signal average (or level of image non-uniformity) for a single image is reasonably small even with the use of an image intensifier. For example, there is greater than 99% probability that any given pixel's signal is within $\pm 5\%$ of the average signal of the image with uniform illumination. This implies that the final temperature measurements are somewhat insensitive to the non-uniformity correction. (2) The PDFs for the three different intensity levels collapse onto each other for more than three decades of probability values, indicating that the degree of sensor (non-)uniformity is independent of the incident illuminance. These results are similar to previous results found using the CMOS camera alone. Hence, for the results presented in this paper, the sensor spatial non-uniformity is corrected by a single 250-shot average image obtained at an $E \cdot \Delta t$ of 1×10^{-3} lux/s.

It is well-known that at high framing rates, image intensifiers, such as that used in the present study, suffer from charge depletion [73], where the number of photoelectrons generated within the MCP for a given voltage decrease as a function of time as the device is unable to fully recharge between successive frames. In a recent study concerning the examination of CMOS and intensified CMOS camera characteristics, Weber et al. [73] found charge depletion to be both intensity- and framing rate-dependent, in addition to being, surprisingly, camera-specific. In this study, we have examined the charge-depletion characteristics (at 10 kHz) of the high-speed image intensifier used for the present temperature imaging. This is assessed by monitoring the camera signal (in counts) of a sequence of n images at constant illuminance, where the inter-frame spacing is 100 µs. Figure 5 shows the results for four different illumination levels,
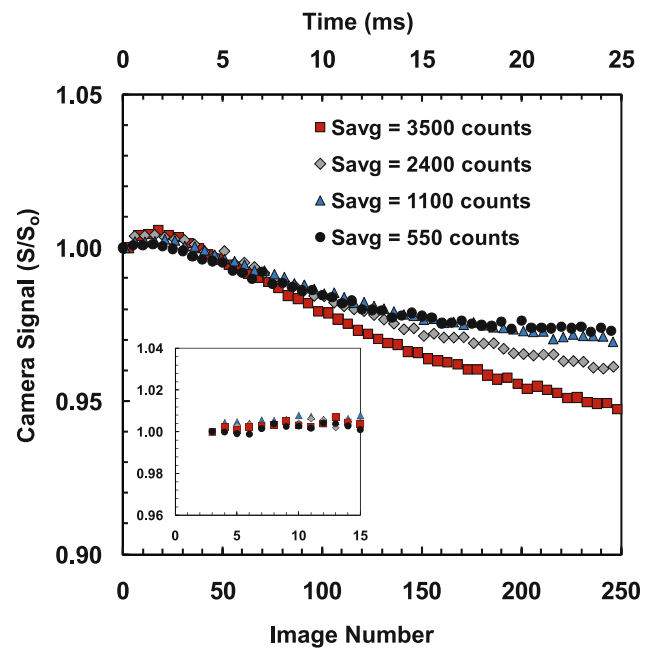

Fig. 5 Normalized camera signal levels (S/S_o) plotted against image number (time) in a sequence of 250 images for a constant gain (as described in text) to examine charge-depletion characteristics of the image intensifier. The images are acquired at 10 kHz and four different illumination levels to show the intensity-dependence on the depletion characteristics at multi-kHz acquisition rates. The four different illumination levels (S_{avg}) correspond to the spatial average over the four pixels indicated in Fig. 3 and the average of 200 independent image sequences. S_o corresponds to S_{avg} for frame 1 of the image sequence. Symbols are plotted for every 10th frame

which results in four different camera signal levels (the average camera signal, S_{avg}, for the cases correspond to 3500, 2400, 1100, and 550 counts, respectively). Each data point represents the average of 200 images over the four pixels indicated in Fig. 3; that is, 200 individual 250-image sequences were acquired to construct the data in Fig. 5. Each data point is normalized by the initial average signal level of the four interrogated pixels (S_o = "frame 1") to show the decrease in signal as a function of time (or number of successive images). Similar to the work in Ref. [73], the depletion shows a dependence on the level of incident luminance (or camera grey level as denoted in [73]). For the lowest level of illuminance (corresponding to $S_{\mathrm{avg}} = 550$ counts), the charge depletion was approximately 2.5% over 250 successive images, which increased to approximately 6% over 250 successively images for the highest illuminance (corresponding to $S_{\mathrm{avg}} = 3600$ counts). For all four cases considered, the results were highly repeatable and no depletion was measured between successive image sequences, that is, S_o was constant (within the noise level of the camera system) for all 200 image sets.

Figure 6 reports the PDF of the depletion levels after 250 successive images at a 10-kHz framing rate for all 1024×664 pixels (6.8×10^5 data points) within a given
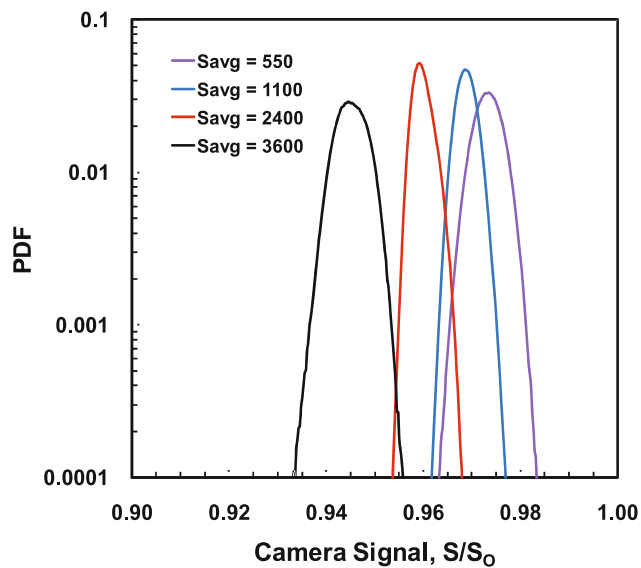
Fig. 6 Probability density function (PDF) of the depletion level after 250 consecutive images for an entire image ($\sim 7 \times 10^5$ data points) for the four different illumination levels shown in Fig. 5. Images are acquired at a 10-kHz. Results indicate that intensity-dependent charge-depletion characteristics are largely pixel independent

image at average camera signal levels of 550, 1100, 2400, and 3500 counts, respectively. In this manner, the initial signal level, S_o, and the frame-dependent signal level, $S(n)$, were monitored for every pixel individually over a series of 250 images. While, S_o or $S(n)$ may vary between individual pixels due to noise, non-uniformity, and non-linearity, Fig. 6 shows that the depletion characteristics (as examined through S/S_o) are largely pixel independent. For all four illuminance levels, there is greater than 99% probability that the pixel-by-pixel variation in S/S_o is less than 1% for the conditions considered in this study.

The insert in Fig. 5 shows the charge-depletion results for the first 10 images, which is equivalent to the record length reported in this manuscript for the high-speed temperature imaging. It is noted that there is no measurable charge depletion over this limited record length and thus no depletion corrections are required for the present imaging studies. However, the data in Fig. 5 (and Fig. 6) demonstrate the need to carefully consider intensity-dependent, charge-depletion correction procedures for future studies with larger image sequence lengths. As described in Ref. [73], it is likely that a pixel-by-pixel, *in situ*, inter-frame referencing and correction procedure will be required that corrects each pixel in the current image based on the pixel's signal (or grey) level in the preceding image.

Image bleed refers to the case where an artifact (or series of artifacts) from one image appear on a subsequent image due to the inter-frame time spacing being comparable or less than the intensifier's phosphor decay time. The current HS-IRO is outfitted with a P47 phosphor which has a reported decay time of the signal down to 1% of 400 ns. Thus, it is expected that image bleed is only significant at acquisition rates exceeding hundreds of kilohertz. Consistent with this assumption, no image bleed was detected (within the resolution of the camera as defined by the noise floor) for 10-kHz acquisition rates.

Shot-to-shot laser pulse energy fluctuations and laser-sheet intensity non-uniformities were determined in two manners: (1) directly from the individual Rayleigh scattering images by measuring the instantaneous intensity magnitude and spanwise spatial distributions in a portion of the image containing only the co-flowing air stream. For a uniform illumination source with constant laser pulse energy, the regions of the co-flowing air (i.e., before the laser sheet propagates into a variable-temperature region) should exhibit a constant signal, both in the laser-sheet spanwise direction encompassing the imaging area and from one image to the next. Thus, any spanwise or pulse-to-pulse variation in signal intensity (in the region of pure air) directly corresponds to a local variation in laser intensity and can be accounted for easily. (2) From a second high-speed CMOS camera ("cam 2" as shown in Fig. 2) that directly images the reflection from the TFP and hence the spatial distribution of the incident laser pulse (and corresponding laser sheet). In this manner, the imaged intensity profile of the laser beam was converted into an equivalent laser-sheet intensity distribution by integrating across the beam, resulting in a 1D array of relative intensity values. The portion of this array corresponding to the Rayleigh imaging region was found by digitally "masking" the upper and lower portions of the 1D array, mapping them to 664 pixel-equivalent units (the number of vertical pixels in the Rayleigh scattering camera), and then comparing the relative intensity distribution (from cam 2) with the corresponding intensity distribution from Rayleigh scattering in air at the measurement volume. By minimizing the residual between the intensity distribution from the measurement volume using the actual sheet-forming optics and the 1D array determined from cam 2, the "sheet profiles" from the external CMOS detection approach (cam 2) can be mapped onto the Rayleigh imaging region. This approach was performed successfully as there were no identifiable differences between intensity profiles determined directly from the measurement volume and the external detection approach.

The first method is preferred in all axial and radial position that contain a consistent region of the uniform, co-flowing air stream as it provides an optimal energy/intensity distribution fluctuation correction. However, for portions of the flame that do not contain a region of the co-flowing air stream (i.e., on "centerline" at conditions in the farfield of the flame), correction method 1 cannot be applied and correction method 2 must be applied. For the results presented in this paper, the imaging regions contained a region of the

uniform, co-flowing air stream, thus correction method 1 was implemented.

3.6 Spatial and temporal resolution

In order to accurately measure scalar properties such as temperature (and temperature fluctuations), the experimental setup must produce sufficient spatial and temporal resolution such that the smallest characteristic scalar length and time scales are adequately resolved. Spatial resolution requirements dictate that the laser probe volume and detector resolution are smaller than the smallest relevant scales at which scalar fluctuations occur and temporal resolution[1] requirements dictate that the measurement acquisition rate is faster than the highest scalar fluctuation frequencies within the flowfield.

Resolution requirements for scalar measurements are usually given as the Batchelor scale [74], which was determined on the basis of *dimensional reasoning* as

$$\lambda_B = \left(\frac{\nu D}{\langle \varepsilon \rangle}\right)^{1/4} = \lambda_K Sc^{-1/2} \tag{5}$$

where ν is the kinematic viscosity, D is the mass diffusivity, $\langle \varepsilon \rangle$ is the mean rate of kinetic energy dissipation, λ_K is the Kolmogorov microscale, and $Sc = \nu/D$ is the Schmidt number. It is common to express the Batchelor scale in terms of outer-flow variables by using measurements, from non-reacting flows [75, 76] to relate $\langle \varepsilon \rangle$ to characteristic large (or outer-) scale velocity and length scales. For example, if the characteristic outer-scale velocity is taken as the centerline velocity (U_c) and the characteristic outer-scale length scale, δ, is taken as the full width at half maximum of the velocity profile of a jet, the Batchelor scale can be expressed as

$$\lambda_B = 2.3\delta Re_\delta^{-3/4} Sc^{-1/2} \tag{6}$$

where $Re_\delta = U_c \delta / \nu$.

Alternative length scales such as the dissipative length scale (λ_D) have been suggested as the appropriate smallest scales necessary for resolving scalar fluctuations and even the dissipation rate of various scalars e.g., [77–80]. The dissipative length scale, which is expressed as

$$\lambda_D = \Lambda\delta Re_\delta^{-3/4} Sc^{-1/2} \tag{7}$$

is defined as the ratio of the smallest length scale over which mixing occurs to the largest fluid mechanical length scale.

Based on measured scalar dissipation rate layers in non-reacting (gas and liquid) flows, Buch and Dahm [77, 78] have reported the scaling constant Λ as 11.2, which is generally accepted within the literature. It is noted that the dissipative length scale is proportional to the Batchelor length scale, but somewhat larger ($\lambda_D = 4.9\lambda_B$), which would relax the resolution requirements of any given experiment.

Mi and Nathan [81] recently assessed spatial resolution requirements in non-reacting heated jets. Their results indicated that resolving the dissipative scale, λ_D, was sufficient for scalar and scalar variance measurements, but in order to accurately measure scalar dissipation rate measurements, the spatial resolution of the measurement should be approximately two times the Batchelor scale. If the same resolution requirements are used for reactive scalars in turbulent flames, then the temperature and temperature fluctuation fields should be sufficiently resolved with an experimental setup that resolves λ_D and only the thermal dissipation rate would necessitate resolving λ_B. More recently, Kaiser and Frank [82–85] have performed high-resolution imaging studies of the dissipative structures within turbulent non-reacting jets and the same DLR flames presented in this study. In these studies, they directly measured the "cutoff" wavelength (λ_C) of the dissipation spectrum within the turbulent flows and flames as well as the dissipation layer widths (λ_D) in flames. The cutoff wavelength (λ_C) is a measure of the fine-scale turbulence and based on Pope's 1-D model spectrum, is denoted as the spatial frequency corresponding to 2% of the peak power spectral density of the dissipative spectrum. Above this spatial frequency, it is estimated that there is less than a 2% contribution to the mean dissipation [86]. The results of Kaiser and Frank [82] indicated that λ_C was approximately 20, 12 and 5 times larger than λ_B estimated from (6) on the centerline on DLR Flame A at axial positions of $x/d = 5$, 10, and 20, respectively. These values are similar to the values of $\lambda_D = 11.2\delta Re_\delta^{-3/4} Sc^{-1/2}$ and their own measured values of $\lambda_D = 7.4\lambda_B$ for the same axial positions.

For temporally correlated measurements, the highest scalar fluctuation frequency present within the turbulent flowfield would most likely correspond to a "convective" Batchelor frequency [63], $f_B = \langle U \rangle / (2\pi\lambda_B)$, where $\langle U \rangle$ is the local mean velocity. However, as described previously in Ref. [30], if a temporal analogue of the spatial resolution requirements outlined by Mi and Nathan [81] is used, it may be reasonable to define alternative characteristic fluctuation frequencies (depending on the measurand of interest) such as a "dissipative" frequency, defined as $f_D = \langle U \rangle / (2\pi\lambda_D)$. Simply put, if spatially resolving λ_D is sufficient for accurately measuring temperature or the temperature variance (in space), then acquiring temperature (or temperature fluctuation) data at acquisition rates higher than f_D may be sufficient for temporally resolving the scalar fields as well. Using the two scalar microscales, λ_B and λ_D, as the bounds

---

[1]In this manuscript, "temporal resolution" refers to the ability to accurately track flowfield features (whether physical or chemical) in time; that is, any two successive measurements are temporally correlated. Other common uses of "temporal resolution" refer to the general benefit of laser-based diagnostics, where the laser pulses are short enough (compared to fluid and chemical time scales) to adequately "freeze" the flowfield during the measurement.
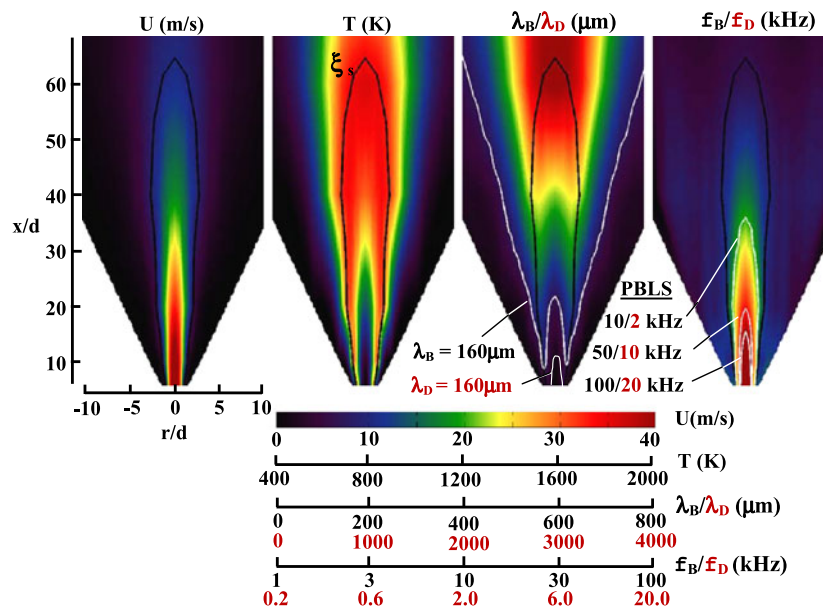
Fig. 7 Estimation of the smallest characteristic scalar length and time scales as a function of spatial position (and temperature) within DLR Flame A. (Left to Right): Re-constructed mean axial velocity field-based point measurements from Ref. [87]; mean temperature field based on the point measurements from Ref. [70]; Batchelor length scale (λ_B) or dissipative length scale (λ_D) as a function of spatial position (the contour corresponding to the limiting spatial resolution of the experimental system as determined by the laser-sheet thickness, LST, is shown in *white*); and the expected characteristic frequencies (bounded by f_B and f_D) as a function of spatial position (various contours corresponding to required acquisition rates are shown in *white*). For each field, the stoichiometric contour, ξ_s, is overlaid with a *solid black line*. One of the benefits of the PBLS is that the inter-pulse spacing can be readily changed to match the necessary temporal resolution as defined by the appropriate characteristic scalar frequency
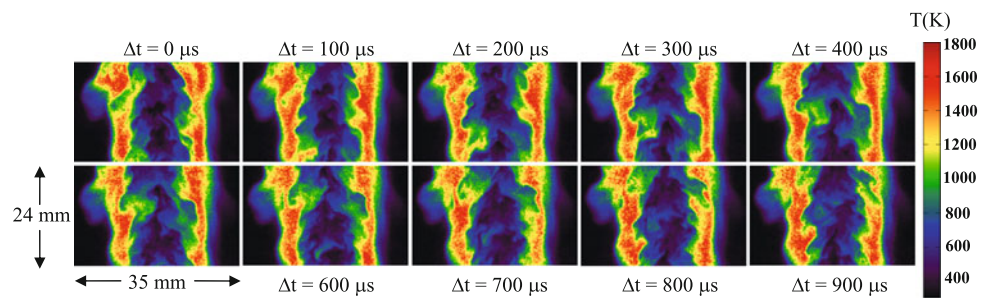
for spatial resolution requirements, the necessary temporal resolution for "tracking" the temperature field in time would be expected to fall between f_B and f_D.

For turbulent flames, λ_B (or λ_D) will vary considerably within turbulent flames due to the temperature-dependent nature of the kinematic viscosity, ν and the corresponding Re_δ. In this manner the characteristic frequencies (f_B or f_D) will vary significantly as well. To illustrate this facet of the turbulent flames and compare with the spatial and temporal resolution of the current measurements and experimental system, two-dimensional maps of estimated values of the smallest length scales (λ_B and λ_D) and characteristic frequencies (f_B and f_D) within DLR Flame A are generated as shown in Fig. 7. The first two fields shown in Fig. 7 represent reconstructions of the average velocity and temperature fields of DLR Flame A based on the point wise velocity measurements from Schneider et al. [87] and the average temperature measurements taken at Sandia, which are part of the TNF database [70]. To calculate λ_B and λ_D (third field shown in Fig. 7), (6) and (7) were used, where the values of U_c and δ were taken from the data of Schneider et al. [87] as shown in the average velocity field in Fig. 7 and the kinematic viscosity was estimated to be that of air at the measured temperature (second field in Fig. 7) according to $\nu(T) = \nu_o(T/T_o)^{1.7}$, where $\nu_o = 1.55 \times 10^{-5}$ m^2/s and $T_o = 300$ K. The characteristic frequencies, f_B and f_D

(fourth field shown in Fig. 7) are then directly calculated from the local mean velocity (as a function of axial and radial position) and the estimated values of λ_B and λ_D. On each field, the average stoichiometric mixture fraction contour, generated from the mixture fraction measurements tabulated in Ref. [70], is overlaid in black.

As mentioned previously, the camera pixel resolution (after 3×3 binning) and the laser-sheet thickness ($1/e^2$ value), which defines the out-of-plane resolution, were both $\sim$160 μm. The contour(s) representing 160 μm is highlighted in white on the λ_B/λ_D map to demonstrate the spatial locations in which the smallest characteristic length scales would be resolved by the current measurements. In terms of resolving the Batchelor scale, λ_B, the current experimental resolution would be sufficient for all radial locations at axial locations of $x/d \geq 20$ and it would be sufficient at the stoichiometric contour for axial locations of $x/d \geq 5$. Furthermore, λ_D is sufficiently resolved for all radial positions for axial locations of $x/d \geq 10$. The temporal resolution of the measurements is determined by the inter-pulse spacing, which can be varied using the PBLS as described in Sect. 3.2. This is one of the key features of the PBLS, that is, the effective repetition rate of the measurements can be systematically increased as test conditions warrant finer temporal resolution such as measurements near the nozzle exit, measurements with increasing Reynolds number,

Fig. 8 Ten-frame, 10-kHz image sequence of the temperature field in DLR Flame A ($Re = 15,200$) at an axial position of $x/d = 10$

4 Sample results and discussion

This section presents sample results obtained using the high-energy laser output from the PBLS at 532 nm to derive temporally correlated image sequences of the temperature field in turbulent non-premixed flames using planar Rayleigh scattering. These measurements are useful for visualizing the dynamics of thermal transport and mixing in "real time" in turbulent flames. Results from the two Reynolds number conditions (DLR A and B) are presented at two axial locations corresponding to $x/d = 10$ and 20, where the images at $x/d = 10$ are centered at $r/d = 0$ and the images at $x/d = 20$ are centered at $r/d = 3$. The accuracy of the temperature measurements is discussed in detail and is assessed

or measurements of dissipation rates. The fourth field presented in Fig. 7 shows an estimation of f_B and f_D as a function of spatial position, placed on a logarithmic scale due to the significant variation of f_B/f_D as a function of spatial position (temperature). Specific f_B/f_D contours associated with various PBLS repetition rates are outlined in "white" to demonstrate the spatial locations in which the smallest characteristic frequencies would be resolved by the current high-repetition-rate measurements. Again, two values are presented to show the necessary operating conditions needed for resolving f_B or f_D, respectively. As an example, in order to resolve f_B at axial locations of $x/d \geq 20$, a 50-kHz repetition rate would be necessary, while a 10-kHz repetition rate would be sufficient for resolving f_D at the same axial locations. In this manuscript, all measurements are presented at a 10-kHz acquisition rate (100 μs spacing) for demonstration purposes. For this repetition rate, f_B is sufficiently resolved for all radial locations at axial locations of $x/d \geq 35$ and is resolved at the stoichiometric contour for all axial locations. Similarly, f_D is sufficiently resolved for all radial positions at axial positions of $x/d \geq 18$ and at the stoichiometric contour for all axial locations. However, it is noted that future work will focus on demonstrating the high-speed temperature imaging at repetition rates exceeding 50 kHz to adequately resolve all characteristic frequencies.

by comparing results from the high-repetition-rate imaging with the published results from the TNF database using 10 Hz Raman/Rayleigh scattering point measurements.

4.1 Example 10-kHz temperature imaging

Figure 8 shows an example of a full ten-frame temporal sequence of 2D temperature images, with inter-pulse spacing of 100 μs, corresponding to the $Re = 15,200$ DLR Flame A case at an axial location of $x/d = 10$. Each image is centered at a radial position of $r/d = 0$ and represents a 24×35 mm field-of-view. Each image has been place on a quantitative scale ($T = 300$ to 1800 K) using (3), where the reference intensity, I_{ref}, corresponds to a region of the co-flowing air stream (not shown in the cropped images of Fig. 8). The variation in the temperature field is represented with a false-color map to highlight the high temperature gradients present throughout the flame. Given the fact that an image intensifier is used and the images are captured at a framing rate of 10 kHz, the image quality of the temperature fields is quite good.

To quantify image quality, the signal-to-noise ratio (SNR) of individual temperature images is determined; first in the co-flowing air stream ($T = 300$ K) by selecting a 450×150 pixel window (before cropping as shown in Fig. 8) and calculating the standard deviation and mean temperature values. For the low-temperature co-flow, the SNR was found to be approximately 35. Since the current flames are highly turbulent, it is somewhat impractical to attempt to find a uniform region within the reaction zones or the burnt gases within the flame to determine the single-shot SNR of the high-temperature regions. In this manner, the SNR can be estimated using a re-formulated version of (9) from Ref. [88], $SNR = S_e/(K S_e G + N_{cam}^2)^{1/2}$, where S_e is the camera signal in units of electrons, K is the gain-dependent noise factor for an intensified camera, G is the electron gain from the photocathode to the sensor, which was determined as 15 as discussed previously, and N_{cam} is intrinsic noise of the camera, which includes the contributions from amplifier, thermal, dark-current shot, and quantization noise from the A–D converter. Since the SNR of the temperature measurements was derived in the co-flow (for a known S_e), the parameters K and N_{cam} are determined directly for the current

Fig. 9 Ten-frame, 10-kHz image sequence of the temperature field in DLR Flame B ($Re = 22,800$) at an axial position of $x/d = 10$
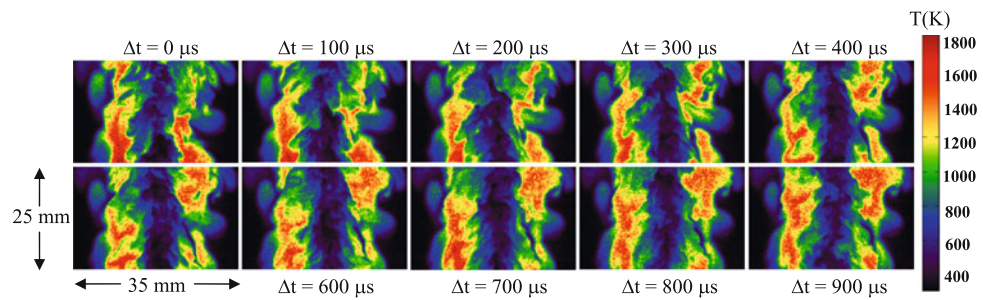

Fig. 10 Ten-frame, 10-kHz image sequence of the temperature field in DLR Flame A ($Re = 15,200$) at an axial position of $x/d = 20$. Images are centered at $r/d = 3$
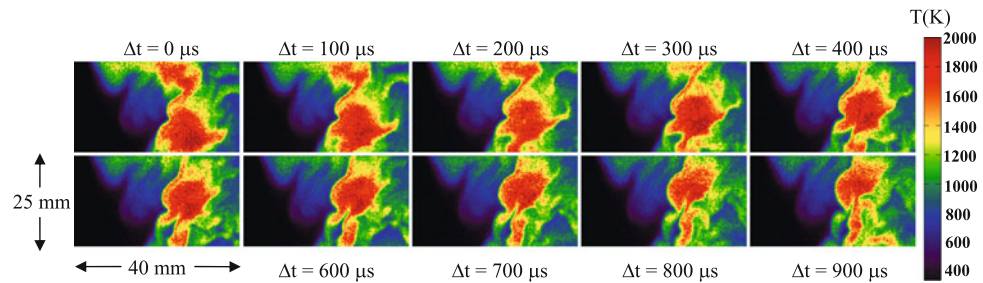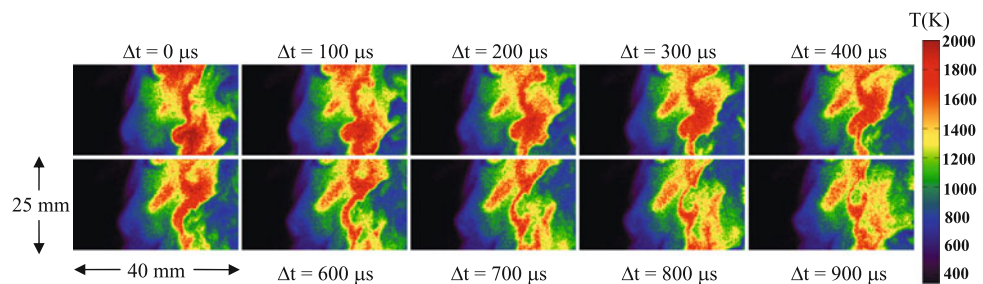

Fig. 11 Ten-frame, 10-kHz image sequence of the temperature field in DLR Flame B ($Re = 22,800$) at an axial position of $x/d = 20$. Images are centered at $r/d = 3$

camera configuration. Furthermore, since the Rayleigh scattering signal scales inversely with temperature (for a constant scattering cross section), S_e at any temperature, T, is estimated as $S_e(T) = S_e(300 \text{ K}) \cdot 300/T$. Using these relations, the SNR at 2000 K is estimated at 13 for the current set of measurements.

However, the most important aspect of these images is not the spatial quality (as conventional, low-repetition-rate, single-shot measurements using CCD cameras achieve higher signal-to-noise ratios as indicated in our earlier work in non-reacting jets [30]), but the temporal correlation of the images, that is, the ability to track the turbulent temperature field and flame dynamics in "real time". For example, Fig. 8 (and other similar acquired image sequences) reveals that at an axial position of $x/d = 10$, the high-temperature regions within DLR Flame A are quite continuous, aligned in the axial direction, and remain "laminar-like" as a function of time with little evidence of local flame extinction. This is in stark contrast to the ten-frame, 10-kHz image sequence of the 2D temperature fields shown in Fig. 9, obtained from DLR Flame B ($Re = 22800$) at the same axial and radial positions as shown in Fig. 8. DLR Flame B exhibits highly contorted, wrinkled, and even broken flame segments within the

1-ms record length. Image sequences such as these have the potential to provide a new understanding of the formation of steep thermal gradients and flame holes, thermal mixing, local flame extinction/re-ignition, and general flame dynamics and structure formation.

As an example, it is well-known that DLR Flame B experiences significant levels of local flame extinction (and re-ignition) based on previous point-based temperature/species concentration measurements e.g., [65, 68, 70]. In the image sequence shown in Fig. 9, the time-history of a flame re-ignition mechanism appears to be highlighted. Starting at frame 1, the peak temperatures in the upper right portion of the image are approximately 1200–1300 K, most likely indicating a previous flame extinction event. Proceeding with frame 2 through frame 5, features such as the formation of colder gas pockets surrounded by hot gas ("flame holes") are clearly seen in the upper right portion of the images. Subsequently in frames 6 and 7, there is a rapid engulfment of the "flame holes" by the hot gases and frames 8 through 10 shows the upstream propagation of the high-temperature "flame front".

Figures 10 and 11 show example temporal image sequences for the DLR A and B flames, respectively, at an

axial location of $x/d = 20$ and centered at a radial location of $r/d = 3$. Each image corresponds to a field-of-view of 25×40 mm and each image is separated in time by 100 µs. As expected, the high-temperature regions (i.e., the "reaction zone") are "thinner" and more contorted for the DLR B flame as compared to the DLR A flame due to the higher Reynolds number and increasing levels of strain. However, it is noted that the differences between the image sequence of flame A and that of flame B at $x/d = 20$ do not appear to be as great as in the case of the more upstream conditions at $x/d = 10$ (Figs. 8 and 9). As a final comment on the utility of tracking the flame dynamics, as determined form the turbulent temperature field, when comparing frame 1 and frame 10 in Fig. 11 (DLR Flame B, $Re = 22800$), the two temperature fields are not only temporally uncorrelated, but are very dissimilar in physical appearance (i.e., "structure" and temperature magnitudes). While this is expected intuitively due to the turbulent nature of the flames, this process occurs on time scales less than 1 ms. This highlights the fact that when acquiring "instantaneous" temperature fields with conventional low-repetition-rate ($\sim$10 Hz) imaging, understanding the formation of a given flame structure and subsequently drawing conclusions about complex, time-dependent physical and chemical mechanisms can be quite difficult. Conversely, multi-kHz imaging allows one to visualize the temporally evolving nature of the combustion process and intuitively understand the processes leading to and establishing a given flame structure. For example, in the sequence shown in Fig. 11, one can see the nominally continuous (although wrinkled), high-temperature zone (peak temperature $\sim$2000 K) in frame 1 is convected downstream (frames 2–6) and thinned (frames 7–10) due to a "bulging" structure, presumably a vortex, thus altering the physical makeup of the flame and lowering the peak flame temperatures to approximately 1600 K.

4.2 Comparison with previous TNF data

To assess the accuracy of the high-speed temperature measurements, the time-averaged temperature field and root-mean square (RMS) of the temperature field at an axial position of $x/d = 20$ are computed and compared to the reference point-based data taken at Sandia National Laboratories, which appears as part of the TNF database for the DLR flames [70]. The TNF data were acquired with simultaneous Raman/Rayleigh scattering and CO laser-induced fluorescence measurements at an acquisition rate on the order of a few Hertz and spatial resolution of 750 µm. Approximately 1000 samples were acquired for each measurement location. For the current high-speed temperature imaging, the mean and RMS temperature values at a given spatial location were extracted from the computed 2D mean and RMS temperature fields based on 120 images. Figure 12 shows the
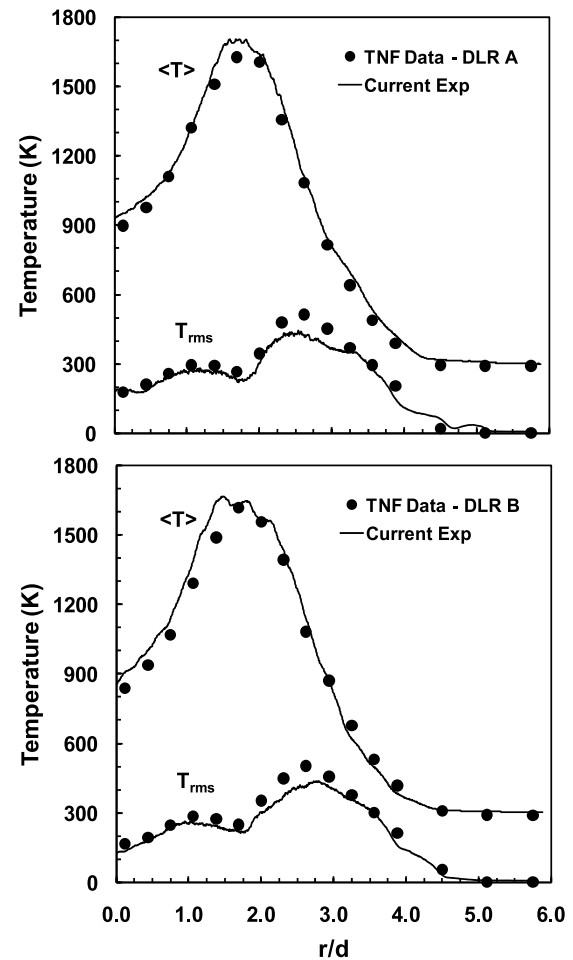

Fig. 12 Comparisons of the time-averaged mean and RMS radial temperature profiles measured at an axial position of $x/d = 20$ in the DLR flames from current high-speed imaging (*solid line*) and the reference point data (*symbols*) from Sandia National Laboratories [70]. (*Top*) DLR Flame A; (*Bottom*) DLR Flame B

comparison between the current high-speed imaging data and the reference data from Sandia for both DLR Flames A and B plotted against the normalized radial position (r/d). As shown in Fig. 12, there is very good agreement between the current high-speed imaging and Sandia reference data for the mean temperature values for both DLR flames, both in terms of temperature magnitude and radial profile shape (mean temperature gradient). In terms of the RMS temperature values, the overall profile shape is computed quite accurately for both flames A and B (including the "dip" at $r/d = 1.75$). However, the current measurements show a peak T_{rms} of approximately 100 K (or $\sim$15%) lower than that of the reference data at $r/d = 2.75$ for both flames. Considering that the mean temperature values and the profile shapes agree favorably between the two data sets, it is hypothesized that the discrepancy between the T_{rms} values stems from the fact that the 120 images used in the present study to deduce $\langle T \rangle$ and T_{rms} is not sufficient to converge

to accurate values of T_{rms}. However, the agreement in the mean temperature values yields an initial indication that the current high-speed temperature images (acquired at 10 kHz) are accurate and quantitative.

5 Conclusions and future work

In this study, we have described the development of quantitative, high-repetition-rate (e.g., 10-kHz) Rayleigh scattering imaging as applied to turbulent non-premixed flames to deduce high-speed image sequences of time-varying, two-dimensional temperature fields. High pulse energies (up to 200 mJ/pulse) at 532 nm are produced from the custom pulse-burst laser system (PBLS) at Ohio State University allowing high-speed planar Rayleigh scattering measurements to be extended into reacting flows for the first time. The combination of the high-energy output of the PBLS and a user-calibrated intensified-CMOS camera allow quantitative temperature imaging. Example image sequences were presented from two well-characterized turbulent jet flames, DLR flames A and B, which are target flame cases within the TNF workshop [70]. The image sequences provided the opportunity to observe the flame dynamics in "real time" including example local extinction and re-ignition sequences. In addition, by comparing the temporally correlated sequences between the two flames, it was possible to examine significant differences in flame dynamics (as deduced from the time-varying temperature field) between flames A and B, which are at two different Reynolds number, with flame B being close to blowout. As an example, it was observed that the high-temperature regions within DLR flame A remain fairly continuous, laminar-like, and aligned in the axial direction, while the structure of DLR flame B is highly contorted and wrinkled and experiences high levels of local flame extinction per image sequence.

Comparisons of mean temperature values from the current high-speed temperature imaging and reference point data acquired at Sandia National Laboratories showed good agreement. This result provides an initial indication that if carefully calibrated, the non-linearity, non-uniformity, and other associated challenges that characterize CMOS- and intensified CMOS-based camera systems can be accounted for and quantitative kilohertz-rate temperature imaging can be performed. High-speed temperature image sequences such as those presented in this manuscript have the potential to yield new information on turbulence-chemistry interaction and important time-dependent processes including auto-ignition, flame extinction/re-ignition, thermal mixing, and highly temperature-dependent kinetic processes such as NO_x formation and fuel consumption rates.

In terms of future work, it is noted that while smaller-scale features and large thermal gradients are quite evi-

dent (especially in the jet core), the use of the image intensifier does degrade the ability to resolve the smallest-scale features that have been observed previously using high-resolution temperature imaging in the DLR flames using scientific-grade CCD cameras e.g, [82–85]. In addition, the use of an image intensifier adds an increasing level of "noise" to the temperature images that will make the determination of thermal gradients and dissipation rates very difficult. Near-term works includes both the development of a new PBLS with much higher pulse energies and the introduction of an optimized collection geometry so that high-speed Rayleigh scattering-based temperature imaging may be performed without the use of an image intensifier similar to our previous work on high-speed mixture fraction imaging in non-reacting jets [30]. Other areas of work include increasing the acquisition rates beyond 50 kHz in order to adequately resolve the thermal fluctuations at upstream axial locations and at higher Reynolds numbers indicative of realistic combustion flow fields.

References

1. N. Peters, Prog. Energy Combust. Sci. **10**, 319 (1984)
2. N. Peters, Proc. Combust. Inst. **21**, 1231 (1986)
3. R.W. Bilger, Prog. Energy Combust. Sci. **1**, 87 (1976)
4. D. Everest, J.F. Driscoll, W.J.A. Dahm, D. Feikema, Combust. Flame **101**, 58 (1995)
5. G.H. Wang, N.T. Clemens, P.L. Varghese, Proc. Combust. Inst. **30**, 691 (2005)
6. N.M. Laurendeau, Prog. Energy Combust. Sci. **14**, 147 (1988)
7. A.C. Eckbreth, *Laser Diagnostics for Combustion Temperature and Species*, 2nd edn. (Gordon and Breach, New York, 1996)
8. K. Kohse-Hoinghaus, J.B. Jeffries (eds.), *Applied Combustion Diagnostics* (Taylor and Francis, London, 2002)
9. F.-Q. Zhao, H. Hiroyasu, Prog. Energy Combust. Sci. **19**, 447 (1993)
10. D.A. Long, *Raman Spectroscopy* (McGraw Hill, New York, 1977)
11. K. Kohse-Hoinghaus, Prog. Energy Combust. Sci. **20**, 203 (1994)
12. J.W. Daily, Prog. Energy Combust. Sci. **23**, 133 (1997)
13. D.A. Greenhalgh, in *Advances in Non-linear Spectroscopy*, vol. 15, ed. by R.J.H. Clark, R.E. Hester (Wiley, New York, 1988), pp. 193–251
14. M. Aldén, A. Omrane, M. Richter, G. Sarner, Prog. Energy Combust. Sci. **37**, 422 (2011)
15. R. Cattolica, Appl. Opt. **20**, 1156 (1981)
16. R.P. Lucht, N.M. Laurendeau, D.W. Sweeney, Appl. Opt. **21**, 3729 (1982)
17. M.P. Lee, B.K. McMillin, R.K. Hanson, Appl. Opt. **32**, 5379 (1993)
18. J.M. Seitzman, R.K. Hanson, P.A. Debarber, C.F. Hess, Appl. Opt. **33**, 4000 (1994)

19. D. Stepkowski, Prog. Energy Combust. Sci. **18**, 463 (1992)
20. R.W. Pitz, R.J. Cattolica, F. Robben, L. Talbot, Combust. Flame **27**, 313 (1976)
21. J.R. Smith, Rayleigh temperature profiles in a hydrogen diffusion flame. Sandia Report, SAND78-8726 (1978)
22. R.W. Dibble, R.E. Hollenbach, Proc. Combust. Inst. **18**, 1489 (1981)
23. M.B. Long, P.S. Levin, D.C. Fourgette, Opt. Lett. **10**, 267 (1985)
24. D.C. Fourgette, R.M. Zurni, M.B. Long, Combust. Sci. Technol. **44**, 307 (1986)
25. B.S. Thurow, N. Jiang, M. Samimy, W.R. Lempert, Appl. Opt. **43**, 5064 (2005)
26. J.D. Miller, M. Slipchenko, T.R. Meyer, N. Jiang, W.R. Lempert, J.R. Gord, Opt. Lett. **34**, 1309 (2009)
27. N. Jiang, M. Webster, W.R. Lempert, Appl. Opt. **48**, B23 (2009)
28. K.N. Gabet, N. Jiang, W.R. Lempert, J.A. Sutton, Appl. Phys. B **101**, 1 (2010)
29. N. Jiang, R.A. Patton, W.R. Lempert, J.A. Sutton, Proc. Combust. Inst. **33**, 767 (2011)
30. R.A. Patton, K.N. Gabet, N. Jiang, W.R. Lempert, J.A. Sutton, Appl. Phys. B (2011). doi:10.1007/s00340-011-4658-1
31. A. Upatnieks, K. Laberteaux, S.L. Ceccio, Exp. Fluids **32**, 87 (2002)
32. C.M. Fajardo, V. Sick, Proc. Combust. Inst. **31**, 3023 (2007)
33. A.M. Steinberg, J.F. Driscoll, S.L. Ceccio, Exp. Fluids **44**, 985 (2008)
34. B. Böhm, C. Heeger, W. Meier, A. Dreizler, Proc. Combust. Inst. **32**, 1647 (2009)
35. A.M. Steinberg, J.F. Driscoll, S.L. Ceccio, Exp. Fluids **47**, 527 (2009)
36. M. Stöhr, I. Boxx, C.D. Carter, W. Meier, Proc. Combust. Inst. **33**, 2953 (2011)
37. A.M. Steinberg, I. Boxx, C.M. Arndt, J.H. Frank, W. Meier, Proc. Combust. Inst. **33**, 1663 (2011)
38. C. Kittler, A. Dreizler, Appl. Phys. B **89**, 163 (2007)
39. I. Boxx, C. Heeger, R. Gordon, B. Böhm, A. Dreizler, W. Meier, Combust. Flame **156**, 269 (2009)
40. I. Boxx, M. Stöhr, C.D. Carter, W. Meier, Appl. Phys. B **95**, 23 (2009)
41. M. Stöhr, I. Boxx, C.D. Carter, W. Meier, Proc. Combust. Inst. **33**, 2953 (2011)
42. W. Paa, W. Müller, M. Stafast, W. Triebel, Appl. Phys. B **86**, 1 (2007)
43. M.E. Cundy, V. Sick, Appl. Phys. B **96**, 241 (2009)
44. J.D. Smith, V. Sick, Appl. Phys. B **81**, 579 (2005)
45. C.M. Fajardo, J.D. Smith, V. Sick, Appl. Phys. B **85**, 25 (2006)
46. M. Cundy, T. Schucht, O. Thiele, V. Sick, Appl. Opt. **48**, B94 (2009)
47. R.L. Gordon, C. Heeger, A. Dreizler, Appl. Phys. B **96**, 745 (2009)
48. M. Juddoo, A.R. Masri, Combust. Flame **158**, 902 (2011)
49. B. Böhm, C. Heeger, R.L. Gordon, A. Dreizler, Flow Turbul. Combust. **86**, 313 (2011)
50. M. Köhler, I. Boxx, K.P. Geigle, W. Meier, Appl. Phys. B **103**, 271 (2011)
51. C.F. Kaminski, J. Hult, M. Aldén, Appl. Phys. B **68**, 757 (1999)
52. C.F. Kaminski, J. Hult, M. Aldén, S. Lindenmaier, A. Dreizler, U. Maas, M. Baum, Proc. Combust. Inst. **28**, 399 (2000)
53. A. Dreizler, S. Lindenmaier, U. Maas, J. Hult, M. Aldén, C.F. Kaminski, Appl. Phys. B **70**, 287 (2000)
54. C.F. Kaminski, X.S. Bai, J. Hult, A. Dreizler, S. Lindenmaier, L. Fuchs, Appl. Phys. B **71**, 711 (2000)
55. J. Hult, M. Richter, J. Nygren, M. Aldén, A. Hultqvist, M. Christensen, B. Johansson, Appl. Opt. **41**, 5002 (2002)
56. J. Hult, U. Meier, W. Meier, A. Harvey, C.F. Kaminski, Proc. Combust. Inst. **30**, 701 (2005)
57. S. Gashi, J. Hult, K.W. Jenkins, N. Chakraborty, S. Cant, C.F. Kaminski, Proc. Combust. Inst. **30**, 809 (2005)
58. J. Olofsson, M. Richter, M. Aldén, M. Auge, Rev. Sci. Instrum. **77**, 013104 (2006)
59. J. Sjoholm, E. Kristensson, M. Richter, M. Aldén, G. Goritz, K. Knebel, Meas. Sci. Technol. **20**, 025306 (2009)
60. P. Wu, W.R. Lempert, R.B. Miles, AIAA J. **38**, 672 (2000)
61. B.S. Thurow, A. Satija, K. Lynch, Appl. Opt. **48**, 2086 (2009)
62. G.-H. Wang, N.T. Clemens, P.L. Varghese, Appl. Opt. **44**, 6741 (2005)
63. G.-H. Wang, N.T. Clemens, P.L. Varghese, Proc. Combust. Inst. **30**, 691 (2005)
64. G.-H. Wang, N.T. Clemens, P.L. Varghese, R.S. Barlow, Combust. Flame **152**, 317 (2008)
65. V. Bergmann, W. Meier, D. Wolff, W. Stricker, Appl. Phys. B **66**, 489 (1998)
66. T.R. Meyer, G.B. King, M. Gluesenkamp, J.R. Gord, Opt. Lett. **32** (2007)
67. B. Bork, B. Böhm, C. Heeger, S.R. Chakravarthy, A. Dreizler, Appl. Phys. B **101**, 487 (2010)
68. W. Meier, R.S. Barlow, Y.L. Chen, J.Y Chen, Combust. Flame **123**, 326 (2000)
69. N. Jiang, M. Webster, W.R. Lempert, J.D. Miller, T.R. Meyer, C.B. Ivey, P.M. Danehy, Appl. Opt. **50**, A20 (2011)
70. R.S. Barlow, International Workshop on Measurement and Computation of Turbulent Nonpremixed Flames, http://www.ca.sandia.gov/TNF/abstract.html
71. S.E. Bohndiek, A. Blue, A.T. Clar, M.L. Prydderch, R. Turchetta, G.J. Royle, R.D. Speller, IEEE Sens. J. **8**, 1734 (2008)
72. R. Hain, C.J. Kahler, C. Tropea, Exp. Fluids **42**, 403 (2007)
73. V. Weber, J. Brübach, R.L. Gordon, A. Dreizler, Appl. Phys. B **103**, 421 (2011)
74. G.K. Batchelor, J. Fluid Mech. **5**, 113 (1959)
75. G. Taylor, Proc. R. Soc. Lond. **151**, 421 (1935)
76. R.A. Antonia, B.R. Satyaprakash, F. Hussain, Phys. Fluids **23**, 695 (1980)
77. K.A. Buch, W.J.A. Dahm, J. Fluid Mech. **317**, 21 (1996)
78. K.A. Buch, W.J.A. Dahm, J. Fluid Mech. **364**, 1 (1998)
79. L.K. Su, N.T. Clemens, Exp. Fluids **27**, 507 (1999)
80. L.K. Su, N.T. Clemens, J. Fluid Mech. **488**, 1 (2003)
81. J. Mi, G.J. Nathan, Exp. Fluids **34**, 687 (2003)
82. J.H. Frank, S.A. Kaiser, Exp. Fluids **44**, 221 (2008)
83. J.H. Frank, S.A. Kaiser, Exp. Fluids **48**, 823 (2010)
84. S.A. Kaiser, J.H. Frank, Meas. Sci. Technol. **22**, 045403 (2011)
85. J.H. Frank, S.A. Kaiser, J.C. Oefelein, Proc. Combust. Inst. **33**, 1373 (2011)
86. S.B. Pope, *Turbulent Flows* (Cambridge University Press, New York, 2000)
87. C.H. Schneider, A. Dreizler, J. Janicka, Combust. Flame **135**, 185 (2000)
88. N.T. Clemens, *Flow Imaging*, in Encyclopedia of Imaging Science and Technology (Wiley and Sons, New York, 2002)